Photoswitchable anapole metasurfaces

Wang, Wenhao; Srivastava, Yogesh Kumar; Gupta, Manoj; Wang, Zhiming; Singh, Ranjan

2022

Wang, W., Srivastava, Y. K., Gupta, M., Wang, Z. & Singh, R. (2022). Photoswitchable anapole metasurfaces. Advanced Optical Materials, 10(4), 2102284-. https://dx.doi.org/10.1002/adom.202102284

https://hdl.handle.net/10356/156116

https://doi.org/10.1002/adom.202102284

Photoswitchable Anapole Metasurfaces

Wenhao Wang[1,2,3], Yogesh Kumar Srivastava[2,3], Manoj Gupta[2,3], Zhiming Wang[1,*] and Ranjan Singh[2,3,*]

[1]*Institute of Fundamental and Frontier Sciences, University of Electronic Science and Technology of China, Chengdu 610054, China*
[2]*Division of Physics and Applied Physics, School of Physical and Mathematical Sciences, Nanyang Technological University, Singapore 637371, Singapore*
[3]*Centre for Disruptive Photonic Technologies, The Photonics Institute, Nanyang Technological University, Singapore 637371, Singapore*
[*]Email: zhmwang@uestc.edu.cn, ranjans@ntu.edu.sg

Abstract

Nonradiating charge-current configurations have attracted attention in photonics for the efficient localization of the electromagnetic fields. Anapole mode is a unique nonradiating state of light induced by the interference of electric and toroidal dipole that possesses rich physics with potential applications in micro-nanophotonics. Active control of an anapole is essential for design and realization of tunable low energy photonic devices. Here, we experimentally demonstrate an active anapole metamaterial device as a switch for the terahertz waves. The metadevice consists of planar resonators with photoactive inclusions of silicon patches in a hybrid metal-semiconductor configuration. The active element enables dynamic control over the contributions of the multipoles that eventually determine the formation of the exotic anapoles that hosts extreme nonradiative confinement and its active switching into sub-radiative Fano resonance and highly radiative electric dipoles. We further demonstrate two orders of magnitude change in the near-field intensity of the anapole that leads to 201% extinction modulation. The anapole metadevice provides a platform to efficiently

control both the far-field radiation and near-field enhancement in metaoptics, promoting active micro-nanophotonic devices for potential applications in terahertz modulators, lasers, filters, and dynamic near-field imaging.

Introduction

The interaction of electromagnetic waves (light) and matter is at the heart of micro-nanophotonics, and its control has spawned a variety of applications ranging from communication technology to biochemistry.[1-2] The electromagnetic response of matter can be described by the electric, magnetic, and toroidal multipole families, which mainly originate from oscillating charges, loop currents, and poloidal currents, respectively. Tailoring the interplay between different multipoles is an efficient approach to control the electromagnetic radiation characteristics. For example, a directive radiation pattern without backscattering could be obtained by balancing the electric dipole (ED) and magnetic dipole (MD), known as the Kerker condition,[3] which has been generalized for higher-order multipoles.[4] The destructive interference of ED and toroidal dipole (TD) yields an exotic nonradiating anapole mode. The term *anapole* (meaning "without poles" in Greek) was first introduced in nuclear physics by Zel'dovich in 1957 to describe the non-interaction of elementary particles and external electromagnetic fields.[5] It was then generalized to electrodynamics and was first observed at microwave frequencies in 2013.[6] Since ED and TD present identical far-field radiation patterns, the total radiation is suppressed when the two modes are excited with the same radiation magnitude but out of phase, giving rise to the electrodynamic

analogy of anapole. The nontrivial nonradiating feature of anapole is also accompanied by strong field confinement inside the matter. These unique properties endow potential of anapole in the applications of cloaking,[7-8] lasers,[9] and nonlinear enhancement.[10-12]

Controlling the light-matter interactions, including the engineered far-field radiation and near-field enhancement, in an active way is desired for modern multifunctional photonic devices. For instance, terahertz (THz) communication desires high-contrast THz amplitude modulation at ultrafast speed,[13-14] and dynamic near-field imaging requires active tuning of near-field intensity.[15] However, most of the current anapole-assisted works show passive control by modifying the structure configuration,[16-17] in which the device's functionality is fixed after fabrication and cannot be changed afterward. A recent study demonstrates active mode shift utilizing phase-change alloy $Ge_2Sb_2Te_5$ (GST).[18] By altering the GST from crystalline phase to amorphous phase, the dark anapole mode is switched to the bright ED mode in several minutes. More efficient control of anapole mode will add new building blocks of meta-optics and further extend the functionalities of anapole based active photonic devices.

Here we demonstrate an anapole metamaterial switch at the THz frequencies. The silicon patches underneath the gaps of paired split-ring resonators (SRs), which support near nonradiating anapole mode, serve as active elements controlling the structures' charge-current configurations. Similar strategies have been applied to demonstrate

controllable electromagnetically induced transparency (EIT),[19-20] switchable optical chirality,[21] polarization switching and dynamic beam steering,[22-23] and tunable filter.[24] In this work, by optical irradiation of different configurations of silicon patches in a metamolecule, the anapole mode is dynamically switched into electric dipole mode or Fano resonance. High extinction modulation depth η = 201% is experimentally achieved due to two orders of magnitude change in the local near-field enhancement. In contrast to the aforementioned tuning mechanism using GST, the optical scheme demonstrated here enables faster switching time of 554 ps, which could be further decreased to an ultrafast time of few picoseconds by ion irradiating embedded silicon patches,[25-26] or by using other active materials such as Ge,[27] Dirac semimetal,[28] perovskites,[29-30] or superconductors[31] with ultrafast charge carrier relaxation.

Results and Discussion

The detailed configuration of the anapole metamaterial switch is schematically illustrated in **Figure 1a**. It highlights the idea that the far-field terahertz response of the metamaterial can be dynamically controlled by switching the optical pump between "off" and "on" states. Figure 1b shows the optical microscopic (OM) image of the fabricated sample which consists of paired THz symmetric split-ring resonators (PTSSRs) with silicon patches beneath the split-gap. Fabrication details are provided in the experimental section. The magnified image of the unit cell clearly reveals the structural configurations of the metamaterial: the periodic constants in the x and y directions are P_x = 120 μm and P_y = 80 μm, respectively; the width and outer ring's

radius of the PTSSRs are w = 6 and r = 40 μm, respectively; the split-gap size is g = 3 μm and the distance between the mirrored split-ring resonators equals to d = 10 μm. The rectangular silicon patches are slightly larger than the split-gaps for the ease of fabrication and to ensure that the silicon patch connects both ends of the aluminum (Al) split rings. When the metamaterial is illuminated by a terahertz wave with the electric field component polarized along the y-direction, mirrored currents are formed and flow in the PTSSRs (as shown in Figure 1c-ii). These loop currents induce magnetic dipoles which are perpendicular to the xy-plane and directed outward (in the left SR) and inward (in the right SR), forming oscillating loop magnetic fields. Such current configuration is a characteristic feature of anapole, leading to diminished far-field radiation and enhanced near-field intensity in the split-gaps. When irradiated with an optical pump beam (800 nm, 1 kHz, 35 fs), both the silicon patches are photoexcited and the surface current configuration change to that of an ED configuration (Figure 1c-i), causing strong far-field radiation and weak near-field enhancement. Alternatively, only a single silicon patch beneath the split-gap in a metamolecule can be placed (Figure 1c-iii) for the photoexcited anapole to transition into a Fano resonance mode which originates from the interference of ED and MD. The system becomes more radiative, and the electric field is mostly confined in the split-gap without silicon patch.

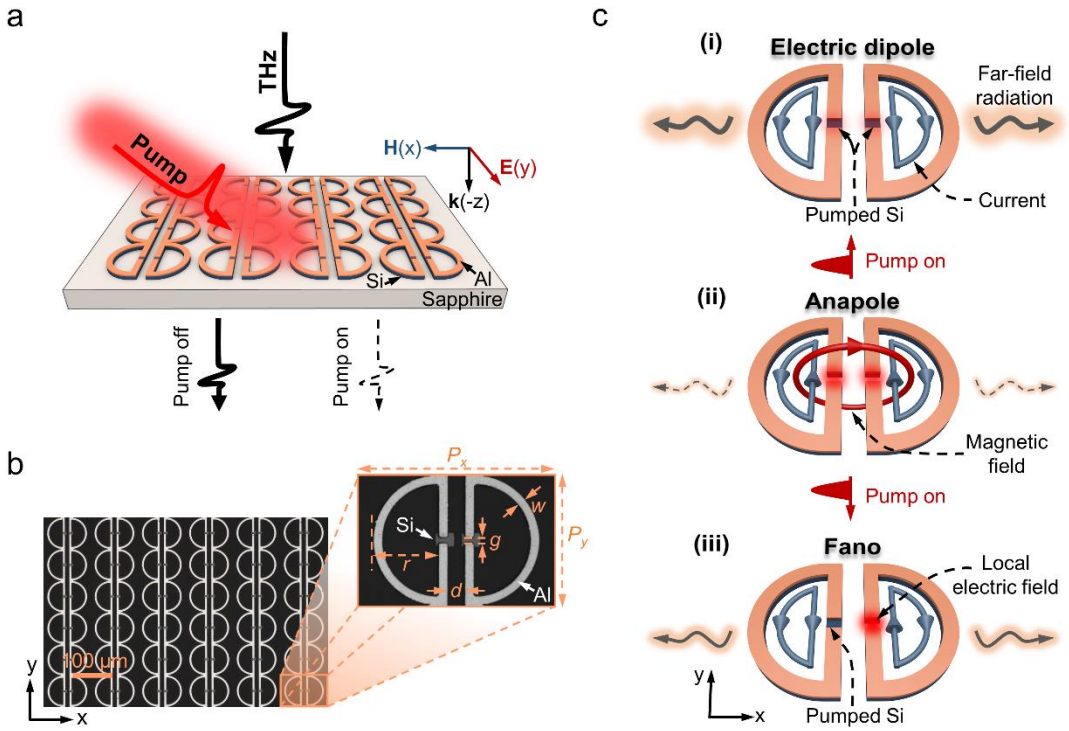

Figure 1. Experiment design of a switchable anapole metadevice. a, Schematic of the anapole metamaterial under the optical pump and THz probe illumination. The transmitted terahertz wave could be controlled by the optical pump. b, Optical microscopy image of the fabricated anapole metamaterial sample. Inset shows the unit cell of the anapole metamaterial consisting of two Al split rings, the split-gaps of which are connected by the underlying silicon patches. The key geometrical parameters of the metamaterial are lattice constant in the *x* and *y* directions, P_x = 120 μm, P_y = 80 μm; outer radius of the rings, r = 40 μm; width of the rings, w = 6 μm; distance between the rings, d = 10 μm; and split gap, g = 3 μm. c, Active control of the far-field radiation and near-field enhancement of a metamolecule by switching c-ii) anapole into c-i) electric dipole or c-iii) Fano resonance. The surface current configurations of different modes, which could be switched by applying an extra optical pump, are illustrated by cyan arrows placed within the split rings.

Before discussing the switching properties of the anapole metamaterial, it would be appropriate to study the origin of the nonradiating anapole mode. The far-field features of the anapole metamaterial are investigated by THz time-domain spectroscopy (THz-TDS) (more details can be found in the experimental section). **Figure 2a** shows the measured extinction spectra of the metamaterial, which is defined as $(1\text{-}T)\times 100\%$, where T is the transmittance from the sample. A notable extinction dip is observed at

0.451 THz, showing the feature of anapole mode. To study the nature of this suppressed radiating state of terahertz wave, numerical simulations are performed using commercial software COMSOL Multiphysics (simulation details are provided in the experimental section). As shown in Figure 2a, the simulated extinction spectra agree well with the measured results. A detailed multipole decomposition of the scattered fields is presented in Figure 2b. Near the valley of the extinction spectra, the ED and TD dominate the scattering power. The toroidal dipole moment **T** has the same far-field radiation pattern as electric dipole moment **P**. In the case of $\mathbf{P} = ik\mathbf{T}$ (derivation could be found in the supporting information), the destructive interference of electric and toroidal dipole moments leads to a non-radiating anapole. The two lower panels of Figure 2b show that at 0.451 THz, the scattered power of ED and TD are identical but out of phase, demonstrating that the anapole mode condition of $\mathbf{P} = ik\mathbf{T}$ is met. We should note that even at the anapole mode, the total scattering is not completely suppressed (Figure 2a). This is because although the far-field radiation induced by ED and TD is canceled, other multipoles, especially magnetic quadrupole (MQ), are excited and lead to non-zero extinction. To get an ideal non-radiative anapole state, the radially polarized source can be used to suppress the multipoles other than ED and TD.[8, 32] Figure 2c shows the calculated magnetic field in the *z*-direction $\mathbf{H_z}$ and surface charge distributions at the anapole mode. A pair of counter-oriented and out-of-plane magnetic dipoles are excited in the SRs, giving rise to a toroidal dipole moment **T** (blue arrow). The oscillating charges accumulated at the ends of the SRs result in an electric dipole moment **P** (red arrow). The destructive interference between the toroidal dipole (**T)** and

electric dipole (**P**), with **P** = *ik***T**, leads to a nonradiating anapole mode with suppressed far-field scattering.

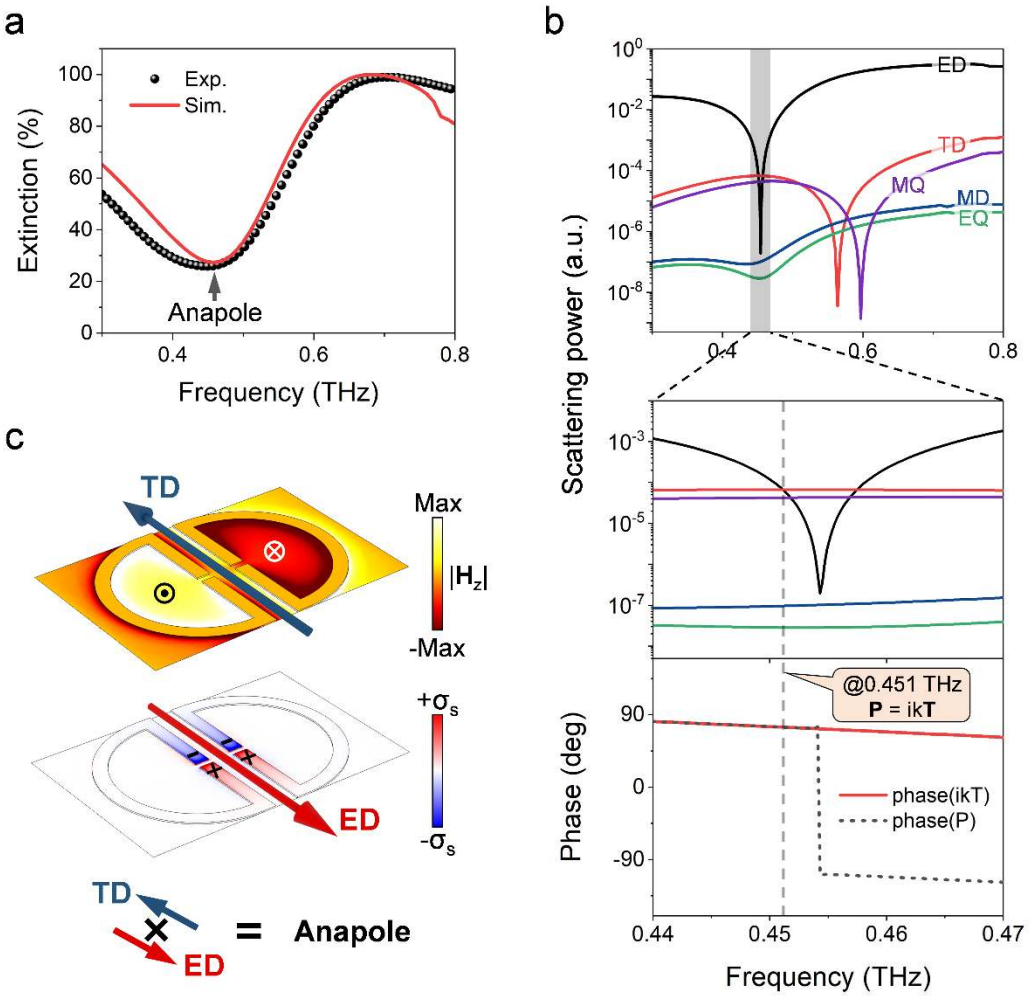

Figure 2. Anapole metadevice features. a, Measured and simulated extinction spectra of anapole metamaterial. b, Calculated far-field scattering power of different multipoles: TD, toroidal dipole; ED, electric dipole; MD, magnetic dipole; EQ, electric quadrupole; MQ, magnetic quadrupole (two upper panels) and phase of electric dipole moment **P** and toroidal dipole moment *ik***T** (lower panel). The scattering power of electric and toroidal dipoles are the same but out of phase at 0.451 THz: **P** = *ik***T**. c, Simulated near magnetic field $\mathbf{H_z}$ and surface charge distributions at 0.451 THz. The destructive interference between toroidal dipole (blue arrow) and electric dipole (red arrow) gives rise to anapole.

The dynamic switching properties of the anapole metamaterial have been investigated by using the optical pump terahertz probe (OPTP) setup, as described in the experimental section. When the energy of the incident photons is larger than the

bandgap of silicon (~ 1.14 eV),[33] the carriers will be pumped from the valence band to the conductive band, providing dynamic photoconductivity and changing the charge-current configuration of the metamaterial. A detailed study of the pump-fluence-dependent photoconductivity of silicon (σ_{Si}) was performed with an unpatterned epitaxially grown silicon on sapphire (SOS) substrate. As shown in the supporting information **Figure S1a**, σ_{Si} increases to 30000 S/m at a large pump fluence of 1274 μJ/cm^2. **Figure 3a** depicts the measured extinction spectra at different pump fluences. As the pump fluence increases, the extinction near 0.451 THz increases and the valley of the extinction spectra becomes shallower and eventually flat, showing the disappearance of the anapole mode. We should note that only a low pump fluence (63.7 μJ/cm^2) is needed to completely switch off the anapole mode, making the anapole metamaterial a promising platform for low-power active photonic devices. The switching time of the device is 554 ps (see supporting information **Figure S2**), which is determined by the accumulation and relaxation feature of the carriers in the SOS substrate. It is much shorter than the switching time of the scheme using phase-change material (4~9 mins),[18] and could be further reduced to less than 20 ps by applying dynamic materials with ultrafast charge carrier relaxation.[27-30] The switching off of the anapole mode is also observed in the simulated extinction spectrum (Figure 3b). Since the measured σ_{Si} only shows a slight dispersion in the studied frequency band 0.3 ~ 0.8 THz (Figure S1a), different pump fluences were modeled in simulation by considering a fluence-dependent σ_{Si} at 0.6 THz for simplicity (Figure S1b). The simulated extinction spectra agree well with the measured results. To clearly understand the switching

behavior, the near electric field and surface current distributions of metamaterial at 0.451 THz for σ_{Si} = 0 and 15000 S/m are calculated and depicted in Figure 3c. At the anapole mode (σ_{Si} = 0 S/m), a counterclockwise (clockwise) loop surface current is formed in the left (right) SR due to the oscillating charges accumulated at the capacitive split-gap. This current configuration generates two counter-oriented magnetic dipoles, giving rise to toroidal dipole moment **T** (Figure 2c). As the anapole formation condition is met by $\mathbf{P} = ik\mathbf{T}$, a non-radiating state is obtained. As σ_{Si} increases to 15000 S/m, silicon is transformed from a semiconductor to a quasi-metal, vanishing the capacitance effect of split-gaps. It thus changes the surface current direction in the rectangular bars of the split-rings and switches the counter/clockwise current configuration to a parallel state. Therefore, the nonradiating anapole mode is switched into a radiative electric dipole mode. In addition, due to the switching-off of the capacitance, only minor confinement of the electromagnetic field occurs in the split-gaps, leading to a sharp drop in the electric field enhancement $|\mathbf{E}|^2/|E_0|^2$, where E_0 is the amplitude of the incident field and **E** is the local electric field. To get a clearer picture of this, the evolution of the $|\mathbf{E}|^2/|E_0|^2$ with the increase of the σ_{Si} is investigated by placing an electric field probe at the center of the split-gap and on the top surface of silicon patch. As shown in Figure 3d, the $|\mathbf{E}|^2/|E_0|^2$ decreases dramatically as σ_{Si} increases due to the shorting of the capacitive split-gaps. Two orders of magnitude change in the $|\mathbf{E}|^2/|E_0|^2$ (from 270 to 2.34) is obtained when the σ_{Si} increases from 0 to 15000 S/m (pump fluence is 637 μJ/cm^2). The optical switch-off of the near-field can be potentially used for dynamic near-field imaging.[15] The relationship between different multipoles'

scattering power at 0.451 THz and σ_{Si} is also studied in Figure 3e. When the optical pump is off (σ_{Si} = 0 S/m), the ED and TD scattering remains identical and dominate over other multipoles. As the photoexcitation pump fluence increases (which is equal to the increase of σ_{Si}), the TD scattering shows a minor change while the scattering power of ED increases gradually and eventually dominates the total scattered power of the metasurface device. A detailed multipole decomposition over the entire bandwidth for different σ_{Si} is provided in the supporting information **Figure S3**. The analysis of the near-field and far-field scattering properties shown above clearly demonstrates the active switching of anapole mode to ED mode.

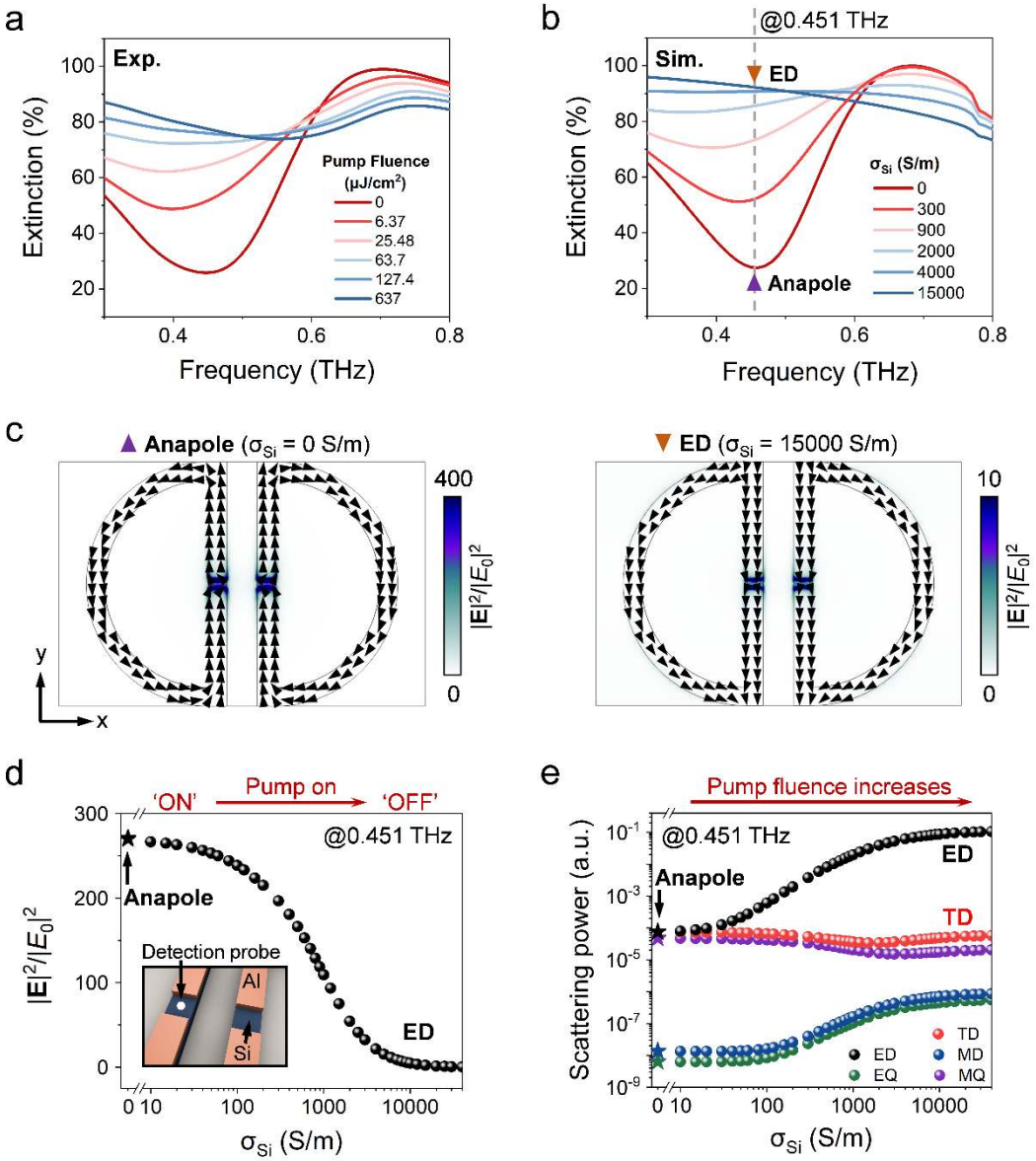

Figure 3. Measured photo-switching of anapole metadevice into an electric dipole. a, Measured and b, calculated extinction spectra of metamaterial at varying optical pump influences, showing the active switching of anapole into electric dipole. c, Electric field distributions of metamaterial for different pump influences at 0.451 THz. The black arrows show the surface currents, forming counterclockwise and clockwise loops in the left and right SRs at the anapole mode, respectively. d, Electric field enhancement $|\mathbf{E}|^2/|E_0|^2$ and e, far-field scattering power of different multipoles variation of metamaterial at 0.451 THz with the change in σ_{Si}. The anapole mode is marked as stars in d and e. Inset in d shows that a detection probe (white dot) is placed in the middle of the gap and at the top surface of the Si patch to obtain the electric field enhancement. By optical pumping of the silicon patches, the near electric field is switched from the 'on' to 'off' state.

The functionality of the anapole metamaterial switch has been further extended by

dynamically photo-switching the anapole into a Fano resonance. **Figure 4a** shows the microscopic image of the fabricated sample, the unit cell of which consists of PTSSRs and one silicon patch beneath the left split-gap. The structural parameters are the same as those shown in Figure 1b. When the optical pump is off, an anapole mode with suppressed extinction is experimentally observed (Figure 4b), which shows a slight redshift compared to Figure 2a. Since the anapole mode originates from the charge-current configuration in the PTSSRs, it is robust to the number of the unpumped Si patches in the system. A multipole analysis is also performed to confirm the anapole mode (see supporting information **Figure S4**). As the pump fluence increases, the far-field radiation of the metamaterial is enhanced, and thus the extinction. When the pump fluence is further increased from 127.4 μJ/cm^2, a resonance dip (noted as Fano I) appears near 0.6 THz and becomes sharper at larger pump fluence. The deviation between the simulated and measured extinction spectra at Fano resonance frequency arises due to the anisotropic dispersion of the *r*-cut sapphire substrate and fabrication imperfections.[34] Detailed information about the effect of the substrate permittivity on the extinction spectra and the robustness of anapole against sapphire's permittivity are provided in the supporting information **Figure S5**. The dynamic switching of anapole mode to Fano I resonance is also observed in the simulation results (lower panel of Figure 4b). The current configurations of different modes are illustrated in the insets. One can note that there is a weak resonance dip (noted as Fano II) at 0.736 THz, which disappears when $\sigma_{Si} \geq 300$ S/m. The Fano II resonance arises from the symmetry breaking induced by the silicon patch beneath the left-hand side split-gap. It is sensitive

to the photoconductivity of the silicon patch and is not observed in the experiments since the intrinsic σ_{Si} is non-zero even in the absence of the photoexcitation.

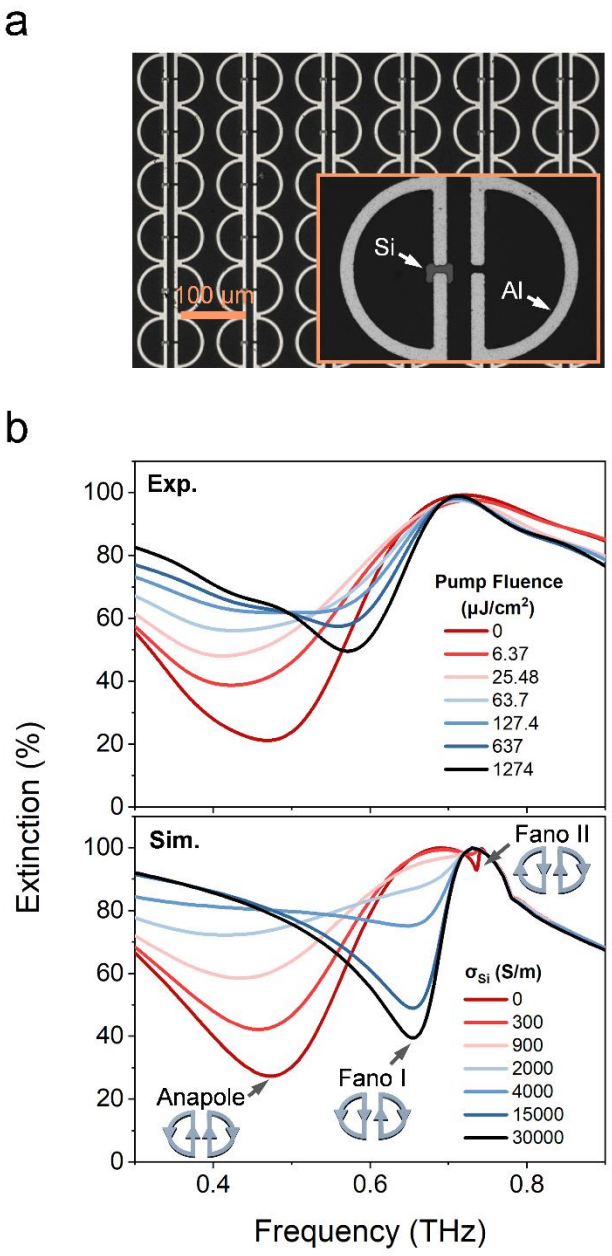

Figure 4. Measured dynamic switching of anapole into the Fano resonance. a, Optical microscopy image of the fabricated anapole metamaterial sample. Inset shows the unit cell of the anapole metamaterial. The gap of the left split ring is connected by the underlying Si patch. b, Measured and calculated extinction spectra of metamaterial at varying optical pump influences, showing the active switching of anapole into Fano I resonance. The insets in the lower panel show the current configurations of different modes.

The near-field and far-field properties of the metamaterial at different resonances are investigated to better understand the mechanism of the mode switching. As presented in **Figure 5a**, mirrored loop currents are observed in the PTSSRs and electric field is enhanced in the split-gaps for anapole mode. When the silicon patch is pumped (σ_{Si} = 30000 S/m), the shorting of the capacitive split-gap converts the counterclockwise configuration of the current in the left SR into a parallel current behavior. The interference between the electric dipole in the left SR and the magnetic dipole in the right SR leads to Fano I resonance with enhanced electric field in the right split-gap. Fano II resonance shows a similar current configuration with Fano I but with the electric field localized in the left split-gap. The evolution of the electric field enhancement at the center of the split-gaps at different frequencies with the increase of σ_{Si} is presented in Figure 5b and 5c. At 0.466 THz, the $|\mathbf{E}|^2/|E_0|^2$ in the left split-gap with silicon patch below is larger than that in the right split-gap for σ_{Si} = 0 S/m, showing asymmetric feature. However, we should note that the surface current still show a mirrored configuration (Figure 5a), and the anapole formation condition is still satisfied (supporting information Figure S4). As σ_{Si} increases, it decreases dramatically and is completely switched off at a large σ_{Si} due to the shorting of capacitive split-gap. However, the $|\mathbf{E}|^2/|E_0|^2$ in the right split-gap decreases first as σ_{Si} increases and finally remains at ~35 owing to the weak excitation of MD. The multipole analysis reveals that the electromagnetic response of the metamaterial is switched from anapole into ED mode (Figure 5d). At 0.65 THz, the electric field shows a similar evolution feature in the left split-gap, while presents an opposite trend in the right gap as σ_{Si} increases. The

strongly excited MD in the right SR at a large σ_{Si} leads to a maximum $|\mathbf{E}|^2/|E_0|^2$ of 580. Figure 5e shows that the entire charge-current configuration of the metamaterial is transformed from ED to electric quadrupole (EQ) mode. A detailed multipole decomposition over the whole studied frequency band for different σ_{Si} is provided in the supporting information **Figure S6**. The different switching behavior of the maximum electric field enhancement in the metamaterial at 0.466 and 0.65 THz endows the device a unique potential for bi-channel dynamic near-field imaging, where the near-field image is 'off' at 0.466 THz and is 'on' at 0.65 THz when the device is optically pumped with high fluence.

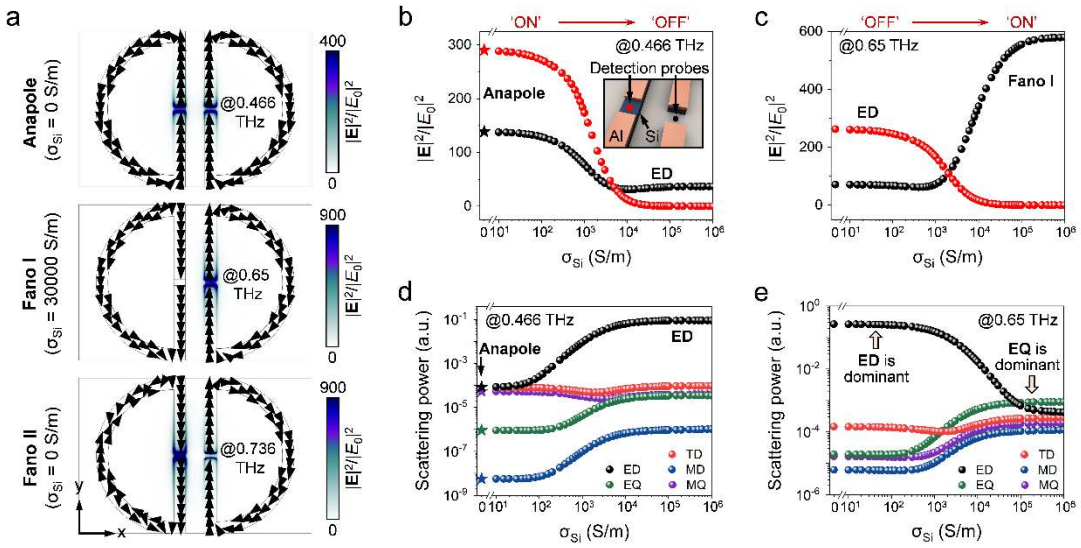

Figure 5. Active tailoring of the near-field and far-field properties of anapole metadevice. a, Electric field distribution of metamaterial at anapole, Fano I, and Fano II resonances. The black arrows show the surface currents. Electric field enhancement variation of metamaterial at b, 0.466 THz and c, 0.65 THz with the change in σ_{Si}. Inset in b shows that two probes are placed in the middle of the left gap and on the top surface of the Si patch (red dot) and in the middle of the right gap over the surface of sapphire (black dot) to detect the electric field. The near electric field can be switched from the 'on' to 'off' state at 0.466 THz and from 'off' to 'on' state at 0.65 THz through optical pumping of the underlying silicon patch. Far-field scattering power of different multipoles variation of metamaterial at d, 0.466 THz and e, 0.65 THz with the change in σ_{Si}. The anapole mode is marked as stars in d and e.

The properties of the anapole metamaterial switch functioning as a modulator have also been investigated. Modulation depth η is one of the important figures of merit. A large η means high electromagnetic response contrast between the "on" and "off" states, which is desired for an ideal modulator. In terms of extinction, η is defined as

$$\eta = \frac{Ext_{\text{on}} - Ext_{\text{off}}}{Ext_{\text{off}}} \times 100\% \quad (1)$$

where Ext_{on} and Ext_{off} represent the extinction of the metamaterial when the optical pump is 'on' and 'off', respectively. **Figure 6** shows the measured η of the anapole metamaterials with silicon patch underneath single and both split gaps in a metamolecule at different values of pump fluences. A maximum η of 201% is achieved near the anapole mode (region shaded in gray) when the two silicon patches in the PTSSRs are pumped with a fluence of 637 μJ/cm^2 (Figure 6a). This originates from the suppressed radiation in anapole mode where Ext_{off} is very small enabling a large modulation depth. In addition to the modulation depth peak, a small dip is also observed for the metamaterial with single silicon patch beneath the PTSSRs, which is because Fano I resonance (region shaded in orange) at high pump fluences (Figure 6b). The modulation time is ~554 ps and it is limited by the slow charge carrier relaxation in intrinsic silicon. By ion irradiating embedded silicon patches,[25-26] or using other active materials with ultrafast charge carrier relaxation,[27-31] the modulation time could be further decreased to an ultrafast time of few picoseconds. The large tuning of the far-field radiation of anapole metamaterial could also be used for achieving other functional metadevices, such as active filters and efficient lasers.

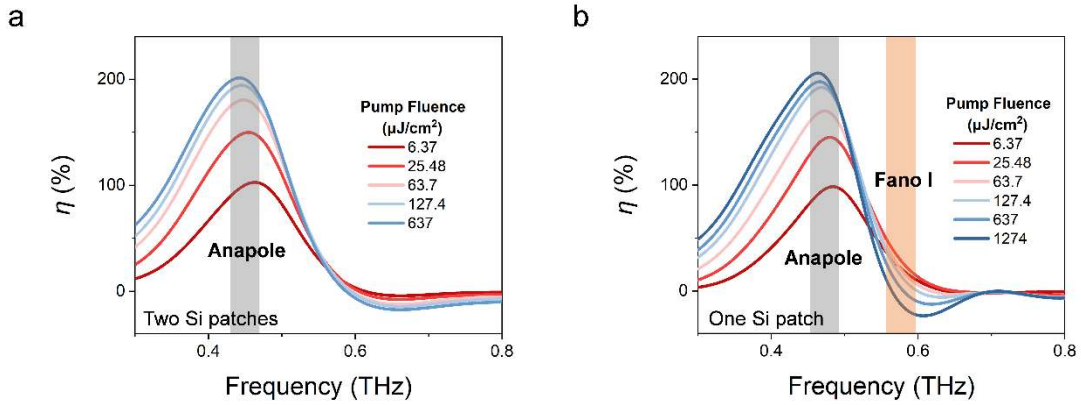

Figure 6. Measured photoexcited modulation at the anapole resonance. Modulation depth $\eta = (Ext_{on} - Ext_{off})/Ext_{off}$ of the measured extinction of anapole metamaterial with a, two Si patches and b, one Si patch in the unit cell. The grey and orange shaded area highlight the anapole mode and Fano I resonance, respectively.

In summary, we have proposed and experimentally demonstrated an anapole metamaterial device for switching and modulation of terahertz waves. The rigorous multipole analysis clearly revealed the dynamic switching of anapole mode with suppressed scattering into radiative electric dipole mode or Fano resonance, through photoexcitation of different configuration of embedded silicon patches in a metamolecule. A large extinction modulation depth of 201% was achieved, suggesting the high practicality of the device for low power switching and modulation applications. We note that although the dynamic switching of anapole mode to electric dipole mode and Fano resonance is through two prototypes. It is possible to achieve multi-mode switching in a single anapole metamaterial. For example, electrically driven cantilevers could be used to control the shorting of the two capacitive split-gaps in a unit cell separately,[35] enabling multifunctional micro-electromechanical system (MEMS)-based anapole metamaterial. Our results offer a new scheme to extensively tuning the radiative scattering and near-field enhancement in active metadevices, and therefore

holds the promise for ultrafast control of anapole-driven lasers, modulators, filters and near-field imaging.

Experimental Section

Sample fabrication: The samples were fabricated by two step conventional photolithography and reactive ion etching (RIE). The PTSSRs were first obtained by depositing a 200 nm thick Al on a silicon-on-sapphire substrate comprising of 600 nm thick silicon epilayer and 476 μm thick *r*-cut sapphire after the first round of UV-illumination based photolithography process. Then, the patterns of the silicon patches were structured by proper alignment of photomask and the second round of photolithography process. The actual silicon patches were obtained by etching undesired silicon from the structure using RIE process and thus leaving the silicon beneath the PTSSRs and split-gaps.

Terahertz time-domain spectroscopy (THz-TDS): The measurements were carried out using ZnTe non-linear crystal based THz-TDS and the transmittance was calculated by $T(\omega) = |E_s(\omega)/E_r(\omega)|^2$, where $E_s(\omega)$ and $E_r(\omega)$ are the Fourier transformed spectra of the sample and reference substrate, respectively. The extinction spectra, defined as the sum of scattering and absorption A, were obtained by $Ext(\omega) = 1 - T(\omega)$ since the scattering is related to the reflectance R in the metamaterial and $1 = A + R + T$.

Optical pump terahertz probe (OPTP) spectroscopy: The dynamic switching performance of the samples was measured using ZnTe THz-TDS and an OPTP spectroscopy setup. A pulsed optical beam was generated from an amplifier laser system (800 nm, pulse width 35 fs, and repetition rate 1 kHz), and then was split into two branches: a transmitted laser beam which pumps the ZnTe crystal for the generation and detection of terahertz radiation and a reflected laser beam working as a pump source. The beam diameter of the optical pump laser is 10 mm and it was larger than the terahertz beam spot size (diameter is 6 mm), ensuring the uniform photoexcitation of the sample. The terahertz probe pulse was delayed by 30 ps (refer to Figure S2) to capture the transmission spectra $t(\omega) = |E_s(\omega)/E_r(\omega)|$ with the maximum modulation.

Simulation: Numerical simulations were performed using commercial software COMSOL Multiphysics. Periodic boundary conditions (PBC) were applied along the *x*- and *y*-direction. Perfectly matched layers (PML) were used at the top and bottom domains. A terahertz wave was incident on the structure with the electric field component polarized along the *y*-direction. The dielectric constant ε_r was set as 11.7 and 10.5 for silicon and sapphire, respectively. The conductivity of the aluminum metal was set as $\sigma_m = 3.7 \times 10^7$ S/m. To investigate the active switching properties of the metamaterial, the conductivity of silicon σ_{Si} was set as the experimentally retrieved photoconductivity of the silicon epilayer at different pump fluences.

Supporting Information

Supporting Information is available from the Wiley Online Library or from the author.

Acknowledgments

W. Wang and Y. K. Srivastava contributed equally to this work. W. W and Z. W acknowledge the support from the National Key Research and Development Program of China (No. 2019YFB2203400) and the "111 Project" (Grant No. B20030). W. W, Y. K. S, M. G, and R. S acknowledge funding support from Singapore NRFCRP23-2019-0005 (TERACOMM). W. W acknowledges the China Scholarship Council for financial support (202006070143).

Conflict of Interest

The authors declare no conflict of interest.

Data Availability Statement

The data that support the findings of this study are available from the corresponding author upon reasonable request.

Keywords

anapole, active switch, modulator, nonradiating, THz metasurface

References

[1] L. Novotny, B. Hecht, *Principles of Nano-Optics*, Cambridge University Press, **2012**.

[2] A. F. Koenderink, A. Alù, A. Polman, *Science* **2015**, 348, 516.
[3] M. Kerker, D. S. Wang, C. L. Giles, *J. Opt. Soc. Am.* **1983**, 73, 765.
[4] W. Liu, Y. S. Kivshar, *Opt. Express* **2018**, 26, 13085.
[5] I. B. Zel'Dovich, *JETP* **1958**, 6, 1184.
[6] V. A. Fedotov, A. V. Rogacheva, V. Savinov, D. P. Tsai, N. I. Zheludev, *Sci. Rep.* **2013**, 3, 2967.
[7] A. K. Ospanova, G. Labate, L. Matekovits, A. A. Basharin, *Sci. Rep.* **2018**, 8, 12514.
[8] L. Wei, Z. Xi, N. Bhattacharya, H. P. Urbach, *Optica* **2016**, 3, 799.
[9] J. S. Totero Gongora, A. E. Miroshnichenko, Y. S. Kivshar, A. Fratalocchi, *Nat. Commun.* **2017**, 8, 15535.
[10] G. Grinblat, Y. Li, M. P. Nielsen, R. F. Oulton, S. A. Maier, *Nano Lett.* **2016**, 16, 4635.
[11] G. Grinblat, Y. Li, M. P. Nielsen, R. F. Oulton, S. A. Maier, *ACS Nano* **2017**, 11, 953.
[12] M. Timofeeva, L. Lang, F. Timpu, C. Renaut, A. Bouravleuv, I. Shtrom, G. Cirlin, R. Grange, *Nano Lett.* **2018**, 18, 3695.
[13] H.-T. Chen, W. J. Padilla, J. M. O. Zide, A. C. Gossard, A. J. Taylor, R. D. Averitt, *Nature* **2006**, 444, 597.
[14] S. H. Lee, M. Choi, T.-T. Kim, S. Lee, M. Liu, X. Yin, H. K. Choi, S. S. Lee, C.-G. Choi, S.-Y. Choi, X. Zhang, B. Min, *Nat. Mater.* **2012**, 11, 936.
[15] J. Li, J. Li, Y. Yang, J. Li, Y. Zhang, L. Wu, Z. Zhang, M. Yang, C. Zheng, J. Li, J. Huang, F. Li, T. Tang, H. Dai, J. Yao, *Carbon* **2020**, 163, 34.
[16] P. C. Wu, C. Y. Liao, V. Savinov, T. L. Chung, W. T. Chen, Y.-W. Huang, P. R. Wu, Y.-H. Chen, A.-Q. Liu, N. I. Zheludev, D. P. Tsai, *ACS Nano* **2018**, 12, 1920.
[17] A. E. Miroshnichenko, A. B. Evlyukhin, Y. F. Yu, R. M. Bakker, A. Chipouline, A. I. Kuznetsov, B. Luk'yanchuk, B. N. Chichkov, Y. S. Kivshar, *Nat. Commun.* **2015**, 6, 8069.
[18] J. Tian, H. Luo, Y. Yang, F. Ding, Y. Qu, D. Zhao, M. Qiu, S. I. Bozhevolnyi, *Nat. Commun.* **2019**, 10, 396.
[19] J. Gu, R. Singh, X. Liu, X. Zhang, Y. Ma, S. Zhang, S. A. Maier, Z. Tian, A. K. Azad, H.-T. Chen, A. J. Taylor, J. Han, W. Zhang, *Nat. Commun.* **2012**, 3, 1151.
[20] Q. Xu, X. Su, C. Ouyang, N. Xu, W. Cao, Y. Zhang, Q. Li, C. Hu, J. Gu, Z. Tian, A. K. Azad, J. Han, W. Zhang, *Opt. Lett.* **2016**, 41, 4562.
[21] M. Liu, E. Plum, H. Li, S. Li, Q. Xu, X. Zhang, C. Zhang, C. Zou, B. Jin, J. Han, W. Zhang, *Adv. Funct. Mater.* **2021**, 31, 2010249.
[22] L. Cong, Y. K. Srivastava, H. Zhang, X. Zhang, J. Han, R. Singh, *Light: Science & Applications* **2018**, 7, 28.
[23] X. Liu, Q. Wang, X. Zhang, H. Li, Q. Xu, Y. Xu, X. Chen, S. Li, M. Liu, Z. Tian, C. Zhang, C. Zou, J. Han, W. Zhang, *Advanced Optical Materials* **2019**, 7, 1900175.
[24] J. Yang, C. Gong, L. Sun, P. Chen, L. Lin, W. Liu, *Sci. Rep.* **2016**, 6, 38732.
[25] D. R. Chowdhury, R. Singh, A. J. Taylor, H.-T. Chen, A. K. Azad, *Appl. Phys. Lett.* **2013**, 102, 011122.

[26] P. Pitchappa, A. Kumar, H. Liang, S. Prakash, N. Wang, A. A. Bettiol, T. Venkatesan, C. Lee, R. Singh, *Advanced Optical Materials* **2020**, 8, 2000101.
[27] W. X. Lim, M. Manjappa, Y. K. Srivastava, L. Cong, A. Kumar, K. F. MacDonald, R. Singh, *Adv. Mater.* **2018**, 30, 1705331.
[28] Z. Dai, M. Manjappa, Y. Yang, T. C. W. Tan, B. Qiang, S. Han, L. J. Wong, F. Xiu, W. Liu, R. Singh, *Adv. Funct. Mater.* **2021**, 31, 2011011.
[29] A. Kumar, A. Solanki, M. Manjappa, S. Ramesh, Y. K. Srivastava, P. Agarwal, T. C. Sum, R. Singh, *Sci. Adv.* **2020**, 6, eaax8821.
[30] M. Manjappa, A. Solanki, A. Kumar, T. C. Sum, R. Singh, *Adv. Mater.* **2019**, 31, 1901455.
[31] Y. K. Srivastava, M. Manjappa, L. Cong, H. N. S. Krishnamoorthy, V. Savinov, P. Pitchappa, R. Singh, *Adv. Mater.* **2018**, 30, 1801257.
[32] J. A. Parker, H. Sugimoto, B. Coe, D. Eggena, M. Fujii, N. F. Scherer, S. K. Gray, U. Manna, *Phys. Rev. Lett.* **2020**, 124, 097402.
[33] B. G. Streetman, S. Banerjee, *Solid state electronic devices*, Prentice-Hall of India, **2001**.
[34] R. Tesař, M. Šindler, K. Il'in, J. Koláček, M. Siegel, L. Skrbek, *Physical Review B* **2011**, 84, 132506.
[35] M. Manjappa, P. Pitchappa, N. Singh, N. Wang, N. I. Zheludev, C. Lee, R. Singh, *Nat. Commun.* **2018**, 9, 4056.